ChemistrySelect

ChemistrySelect
Chemistry Europe
European Chemical Societies Publishing

RESEARCH ARTICLE OPEN ACCESS

Selective Copper Sensing and Imaging With a Pyrroloquinoxaline Probe for Biological and Environmental Applications

Margarita Damai | Priyanka Ganguly | Joshmi Joseph | Natalia Buckler Reinoso | Chris Bax | Daniel Sykes | Bhaven Patel

Applied Chemistry and Pharmaceutical Technology (ADAPT), School of Human Sciences, London Metropolitan University, London, UK

Correspondence: Priyanka Ganguly (p.ganguly@londonmet.ac.uk) | Bhaven Patel (b.patel1@londonmet.ac.uk)

Received: 7 February 2026 | **Revised:** 19 June 2026 | **Accepted:** 29 June 2026

Keywords: fluorometric chemosensor | environmental monitoring | cellular imaging | Cu^{2+} ions | pyrroloquinoxaline

ABSTRACT

Copper is an essential trace element, but dysregulation of copper homeostasis is associated with significant biological and environmental consequences, necessitating sensitive and selective detection strategies for Cu^{2+}. In this study, we report the design and synthesis of a pyrroloquinoxaline (PQ)-based fluorescent probe for rapid detection of Cu^{2+} ions in aqueous and biological media. PQ exhibits pronounced fluorescence quenching upon coordination with Cu^{2+}, enabling sensitive detection with a low limit of detection suitable for trace-level analysis. Spectroscopic studies confirm a 1:1 binding stoichiometry and provide insight into the coordination-induced quenching. The probe displays a preferential response to Cu^{2+} over competing metal ions and performs reliably in real water samples. Confocal fluorescence imaging further confirms the biocompatibility of PQ and its ability to monitor intracellular Cu^{2+} levels in living cells. These results highlight pyrroloquinoxaline-based scaffolds as promising platforms for Cu^{2+} sensing in biological and environmental systems.

1 | Introduction

Copper is an essential trace element that plays a critical role in numerous biological processes, primarily by functioning as a cofactor in various enzymes involved in redox catalysis, connective tissue formation, and mitochondrial respiration [1]. In adult humans, the total body copper content is approximately 80 mg, with reported values ranging from 50 to 120 mg [2, 3]. Disruptions in copper homeostasis are linked to several pathological conditions, including Wilson's disease, hepatic cirrhosis, and neurodegenerative disorders such as Alzheimer's and Parkinson's disease [4, 5]. In its ionic form (Cu^{2+}), copper exhibits versatile reactivity and catalytic properties, making it widely applicable across industrial, agricultural, and chemical sectors. Despite its utility, excessive copper accumulation poses significant risks to biological systems. Elevated Cu^{2+} levels can be toxic to animals, plants, and microorganisms [6, 7]. In humans, abnormal copper levels contribute to disease [8], while in the environment, copper contamination, particularly in aquatic ecosystems, represents a persistent challenge [9].

Copper enters freshwater systems through various anthropogenic sources, including mining discharge, industrial effluents, and corrosion of domestic plumbing. Regulatory bodies such as the World Health Organisation (WHO) have established a guideline value of no more than 31.4 μM for Cu^{2+} in drinking water to mitigate health risks [10]. Excessive copper accumulation has been shown to disrupt ecological stability and pose serious risks to food safety [11–13]. Given its dual role as both a vital nutrient and a potential contaminant, the ability to

sensitively and selectively detect Cu^{2+} in environmental and biological systems is of considerable biomedical and ecological importance.

Current analytical techniques for copper detection, such as atomic absorption spectroscopy (AAS), inductively coupled plasma mass spectrometry (ICP-MS), atomic emission spectroscopy (AES), and voltammetry, offer high accuracy and sensitivity [14–16]. However, their reliance on sophisticated instrumentation, labor-intensive sample preparation, and centralized laboratory infrastructure limits their applicability for real-time analysis [6]. In contrast, fluorescent chemosensors present an evolving alternative due to their operational simplicity, low cost, high sensitivity, specificity, and nondestructive analysis [17–24].

In recent years, considerable progress has been made in Cu^{2+} detection technologies, with a range of electrochemical sensors reported based on nanostructured materials, conductive polymers, and hybrid interfaces [25–27]. These systems offer high sensitivity and are attractive for portable and field-deployable monitoring. However, electrochemical approaches often require electrode modification, frequent calibration, and may suffer from surface fouling or limited applicability in complex biological matrices. By comparison, fluorescence-based probes enable real-time, nondestructive detection with high spatial resolution, making them especially suitable for intracellular imaging and environmental analysis. Despite these advantages, the development of fluorescent sensors that combine high selectivity, low detection limits, and applicability across both environmental and biological systems remains an ongoing challenge.

4-Substituted pyrroloquinoxaline derivatives have emerged as versatile fluorescent probes with applications in environmental sensing, ion detection, and biomedical diagnostics. Their rigid, conjugated structures and tuneable donor–acceptor properties enable strong fluorescence and selective analyte recognition. Karpe et al. reported that pyrroloquinoxaline-based fluorophores exhibit static fluorescence quenching upon interaction with nitroaromatics, achieving micromolar detection limits [28, 29]. Hydrazone derivatives of pyrroloquinoxalines have been shown to selectively bind amyloid fibrils and prion aggregates, demonstrating dual functionality as diagnostic and therapeutic agents in prion disease models [30, 31]. Additionally, thiophene-derived pyrroloquinoxalines have shown nanomolar sensitivity and high selectivity for sodium ions [32]. These studies collectively highlight the potential of pyrroloquinoxaline scaffolds as modular platforms for the development of targeted, high-performance fluorescent sensors tailored to diverse chemical and biological analytes.

Given the significant health and environmental implications of copper, there remains a need for simple yet highly selective fluorescent probes that operate effectively across both environmental and biological systems while providing mechanistic insight into metal-ligand interactions. To address the need for accessible and reliable copper detection, we have developed 2-(pyrrolo[1,2-a]quinoxalin-4-yl) pyridine (PQ), a fluorescence-based probe capable of rapid, selective, and sensitive recognition of Cu^{2+} ions. The probe exhibits a low limit of detection (LOD), making it suitable for monitoring trace levels of Cu^{2+}. The coordination process was characterized using Job's plot, Benesi–Hildebrand analysis, and ^{1}H-NMR spectroscopy, providing insight into the binding mechanism.

Unlike many existing Cu^{2+} sensors that are restricted to either environmental or biological applications, PQ demonstrates reliable performance in real-world water samples as well as in living cells. Importantly, PQ demonstrated practical applicability in real-world water samples, where fluorescence-based detection offers distinct advantages such as operational simplicity, minimal sample preparation, and potential for on-site analysis. In addition, cellular imaging experiments confirmed that PQ can detect Cu^{2+} in living cells, underscoring its potential as a tool for investigating copper-associated biological processes and contributing to a deeper understanding of its roles in health and disease.

By integrating selective Cu^{2+} recognition, mechanistic understanding, and dual environmental–biological applicability within a single molecular scaffold, this work highlights pyrroloquinoxaline derivatives as a promising and underexplored platform for next-generation fluorescent metal ion sensors.

2 | Materials and Methods

2.1 | Synthesis of 2-(Pyrrolo[1,2-a]quinoxalin-4-yl) Pyridine (PQ)

Pyridine-2-carboxaldehyde (0.11 mL, 1.2 mmol) and 1-(2-aminophenyl) pyrrole (158 mg, 1.0 mmol) were added to a solution of *p*-toluene sulfonic acid monohydrate (20 mg, 0.1 mmol) in ethanol (2 mL) and stirred at 25°C for 15 min. The reaction was monitored by TLC until complete consumption of starting materials was observed. The mixture was treated with $KMnO_4$ (158 mg, 1.0 mmol) and stirred for an additional 20 mins at 25°C. The reaction mixture was concentrated under reduced pressure. The residue was treated with saturated aqueous $NaHCO_3$ solution (5 mL) and extracted with ethyl acetate (3 × 5 mL). The organic layers were combined, washed with water (3 × 50 mL), dried over anhydrous sodium sulfate and concentrated under reduced pressure. The crude reaction mixture was purified by column chromatography (9:1 Hex:EtOAc) to afford PQ (104 mg, 66%) as a yellow solid. m.p. 105°C–107°C; ν_{max}/cm^{-1} (neat) 3058, 2934, 1574, and 1536; δ_H (500 MHz, $CDCl_3$) 8.79–8.84 (1H, m, ArH), 8.43 (1H, dt, *J* 7.88, 1.10, ArH), 7.99 (1H, dd, *J* 2.52, 1.26, ArH), 7.84–7.90 (2H, m, 2 × ArH), 7.77 (1H, dd, *J* 4.10, 1.26, ArH), 7.48–7.53 (1H, m, ArH), 7.38–7.47 (2H, m, 2 × ArH), 6.95 (1H, dd, *J* 4.10, 2.52, ArH); δ_H (500 MHz, CD_3CN) 8.76–8.81 (1H, m, ArH), 8.50 (1H, dt, *J* 7.96, 1.06, ArH), 8.20 (1H, dd, *J* 2.68, 1.42, ArH), 8.09 (1H, dd, *J* 8.35, 1.10, ArH), 7.94–8.01 (2H, m, 2 × ArH), 7.88 (1H, dd, *J* 4.10, 1.26, ArH), 7.61 (1H, ddd, *J* 8.35, 7.09, 1.58, ArH), 7.48–7.54 (2H, m, ArH), 6.98 (1H, dd, *J* 3.94, 2.68, ArH); δ_C (125 MHz, $CDCl_3$) 156.4 (C), 151.1 (C), 148.8 (CH), 136.6 (CH), 135.6 (C), 130.3 (CH), 127.9 (HC), 127.5 (C), 125.0 (CH), 124.6 (C), 124.2 (CH), 123.3 (CH), 114.4 (CH), 114.2 (CH), 113.6 (CH), 110.5 (CH); *m/z* (NSI) 246.1024 $[M+H]^+$, $C_{16}H_{12}N_3$ requires 246.1026.

2.2 | Optical Studies

A standard solution of PQ (6.30 mM) in acetonitrile (ACN) and various metal ions (6.30 mM) in water were prepared separately.

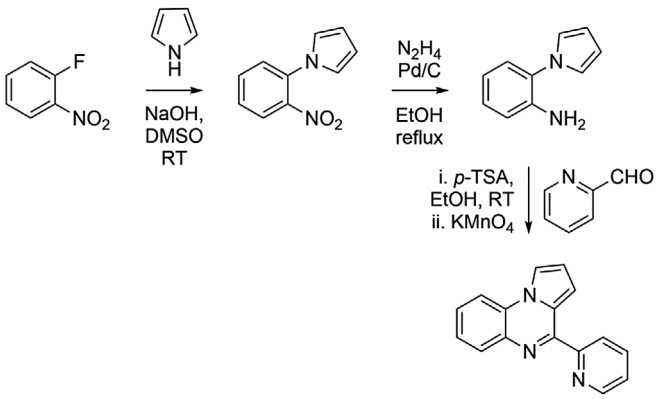

SCHEME 1 | Synthesis of fluorescent probe PQ.

For each titration, PQ (3 mL) was transferred to a cuvette, and prepared metal ions were added and mixed well. The optical properties (UV–vis and fluorescence) were studied at room temperature. A number of fluorescence investigations were conducted, including pH, selectivity, sensitivity, time, temperature, reversibility, and stability. For the pH studies, PBS solutions with pH values ranging from 1 to 11 were prepared and added to the PQ probe. The resulting fluorescence spectra were observed at an excitation wavelength of 320 nm. In order to find out the detectable range, sensitivity studies were done by varying the amount of Cu^{2+}.

3 | Results and Discussion

3.1 | Synthesis of PQ

2-(Pyrrolo[1,2-a]quinoxalin-4-yl) pyridine was synthesized using a three-step procedure from commercially available 2-fluoronitrobenzene, with the key intermediate 1-(2-aminophenyl)pyrrole prepared according to previously reported procedures [33]. A modified Pictet–Spengler reaction between the amino-pyrrole intermediate and 2-pyridinecarboxaldehyde, catalyzed by *p*-TSA, followed by oxidative aromatization with $KMnO_4$ afforded PQ in 66% yield (Scheme 1). The structure of PQ was confirmed by NMR spectroscopy and mass spectrometry (see Section 2).

3.2 | UV–vis Study and Fluorescence Measurements

The optical properties of PQ were investigated using ACN. The UV–vis absorption spectrum indicates maximum absorption (l_{abs}) is observed across 230–290 nm and 320–450 nm (Figure 1a), corresponding to the p–p* transition and intramolecular charge transfer between the aromatic rings [34]. Upon excitation at 380 nm, PQ exhibits a strong fluorescence emission with a maximum (l_{em}) at 485 nm. A bathochromic shift in the absorption peaks is observed on addition of copper analyte (Figure 1b), which is ascribed to the ground-state complex formation by charge transfer from the sensor ligand to the analyte [32]. A pronounced quenching of the emission signal at 450 nm is observed upon copper analyte addition (Figure 1c), suggesting a quick and strong interaction between the PQ sensor and copper ions. Time-resolved fluorescence measurements were carried out to better understand the photophysical behavior of the PQ probe. The fluorescence decay profile of PQ (Figure S4), was analyzed with an exponential fit. The data were well described by a single-exponential decay model, showing a fluorescence lifetime (τ) of 13 ns and a χ^2 value of 1.1, indicating a good fit and a single emissive species.

3.3 | Selectivity and Concentration Study

The interference and selectivity of the sensor were evaluated using 20 different metal ion solutions through a series of fluorescence measurements. The addition of various metal ions caused partial decreases in the fluorescence intensity of PQ, as represented by the yellow bars in Figure 2a. The photographs of the probe solution and the probe-metal ion mixtures can be observed in Figure 2b,c. Images were recorded under both normal daylight conditions and UV illumination to demonstrate the visual changes accompanying the fluorescence response. However, the introduction of copper ions resulted in a markedly stronger fluorescence quenching response, as illustrated by the red bars in Figure 2a. While some response is observed for other metal species, the extent of quenching induced by Cu^{2+} is significantly greater, indicating a preferential sensing response toward Cu^{2+} ions. To ensure a valid comparison, all metal ions, including Cu^{2+}, were examined at the same concentration. Additional competitive experiments were conducted in which Cu^{2+} was introduced together with other common metal ions at identical concentrations, which is standard practice for fluorescence-based selectivity studies. To further verify that this behavior persists in mixed-ion environments, additional competitive experiments were performed in which Cu^{2+} was introduced together with other common metal ions. These measurements showed that coexisting ions did not significantly diminish the Cu^{2+}-induced fluorescence quenching, demonstrating that PQ maintains a high degree of selectivity even under competitive conditions. The observed selectivity is attributed to the electronic configuration and coordination behaviors of Cu^{2+} compared to other metal species [32]. The Cu^{2+} ion's [$3d^9$] configuration allows it to readily bind with nitrogen-rich species like PQ. Additionally, the π-electrons of PQ's quinoxaline ring provide nitrogen lone pairs that can efficiently coordinate with Cu^{2+}, forming a stable complex with either a square planar or distorted octahedral geometry. Cu^{2+} ions are known to cause distortions in the typically octahedral geometry, resulting in a tetragonally elongated structure with two longer bonds along one axis and four shorter bonds in the plane, a phenomenon known as the Jahn–Teller effect [35, 36]. The donor environment and geometrical flexibility of PQ are well-suited to accommodate this distortion, resulting in stronger coordination interactions and enhanced fluorescence quenching. To further evaluate the selectivity of PQ toward different oxidation states of copper, fluorescence responses were measured in the presence of both Cu^{+} and Cu^{2+} salts. Copper(I) chloride (CuCl) and copper(I) bromide (CuBr) produced negligible changes in fluorescence intensity, whereas copper (II) chloride ($CuCl_2$) and copper (II) sulfate ($CuSO_4$) induced pronounced fluorescence quenching (Figure S5). These observations demonstrate a strong preference for Cu^{2+} over Cu^{+}, attributable to the higher coordination number and stronger

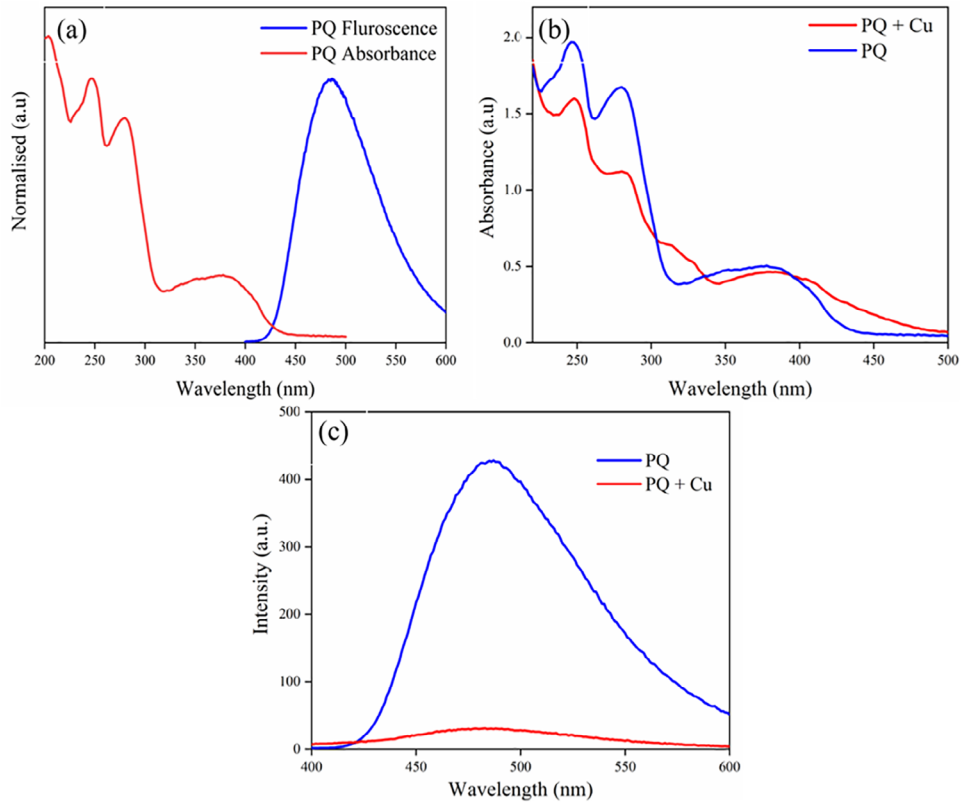

FIGURE 1 | (a) Normalized fluorescence emission and UV–vis absorption spectrum of PQ sensor. (b) UV–vis absorption of PQ (6.3 mM) and PQ with copper (20 mM), and (c) fluorescence emission of PQ and PQ with copper.

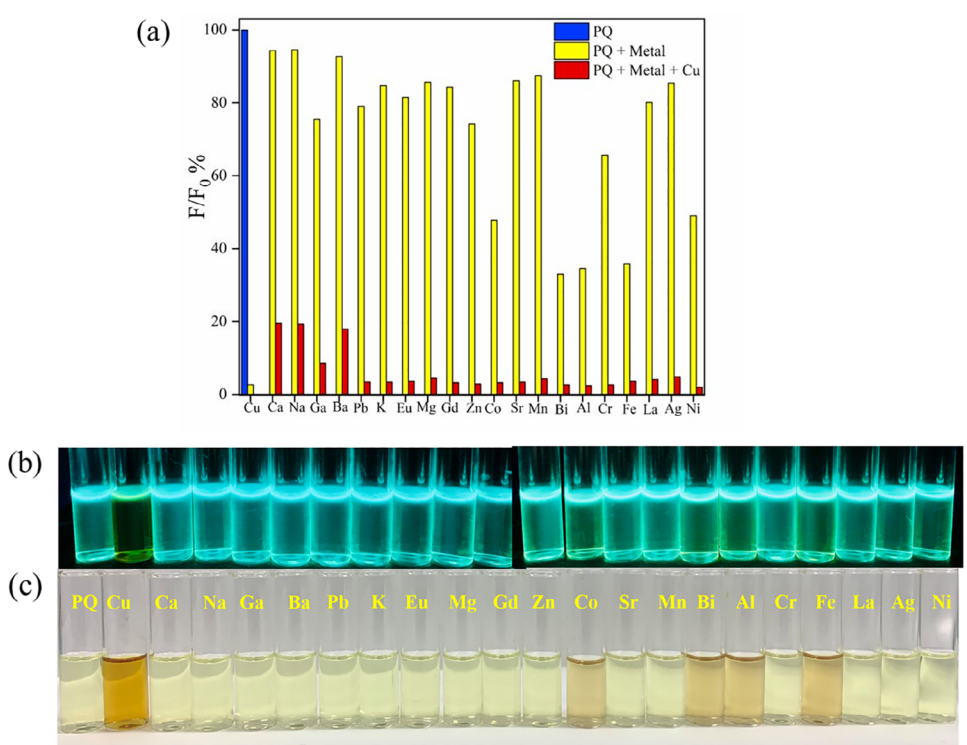

FIGURE 2 | (a) Fluorescence emission intensity of PQ (blue), PQ + metal ion (yellow), and PQ + metal ion with the addition of 10 mM of copper (red). (b) Digital photographs of PQ and PQ + Cu^{2+} solutions recorded under daylight conditions. (c) Digital photographs of PQ and PQ + Cu^{2+} solutions recorded under UV light.

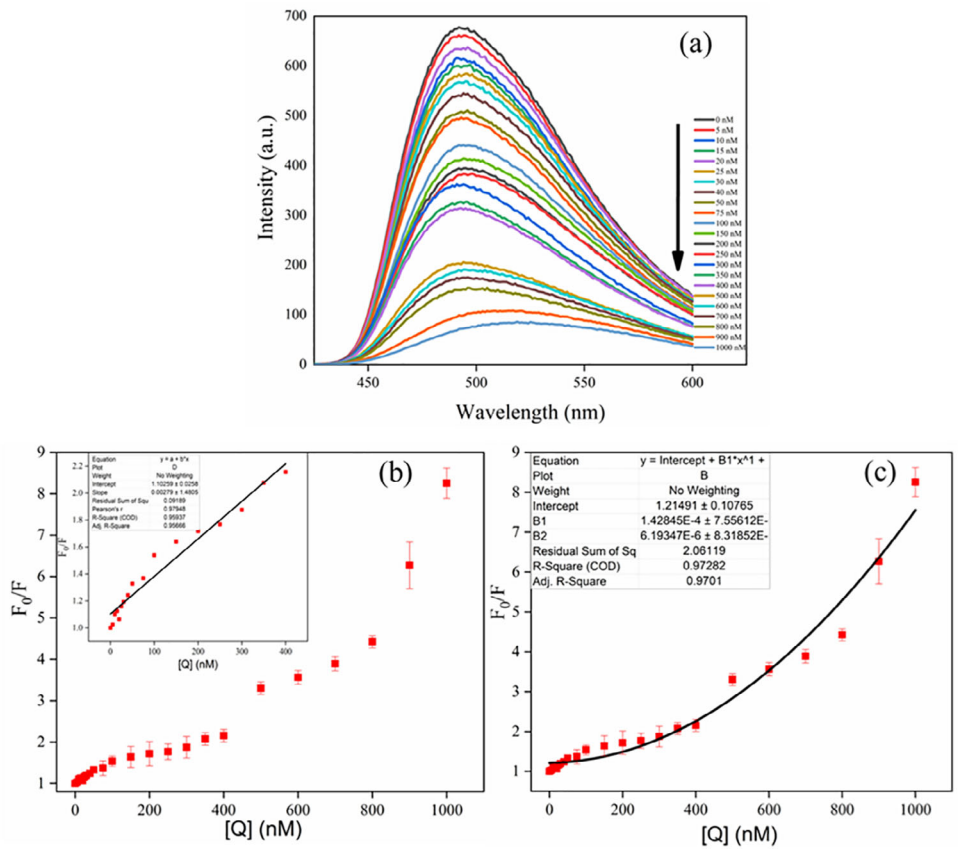

FIGURE 3 | (a) Concentration study, (b) Stern–Volmer quenching plot, and (c) second-order polynomial fitted plot.

Lewis acidity of Cu^{2+}, which promote more effective interactions with the donor sites of the pyrroloquinoxaline framework.

The fluorescence quenching behavior of PQ was studied using varying concentrations of copper ions. A gradual decrease in fluorescence intensity was observed at lower metal ion concentrations (Figure 3a), indicating a steady quenching trend. The intensity declines significantly once the concentration exceeds 400 nM, indicating the onset of more pronounced quenching behavior. Notably, beyond 1000 nM, the signal intensity plateaus, displaying minimal change with further increases in metal concentration. This suggests the saturation of the quenching mechanism or the formation of stable complexes that no longer contribute to additional quenching. To further investigate the quenching dynamics, a Stern–Volmer plot was constructed (Figure 3b). The relationship is described by the equation:

$$\frac{F_0}{F} = 1 + K_{SV}\,[Q] \tag{1}$$

where, F_0: initial fluorescence (no metal), F: fluorescence at a given metal concentration, $[Q]$: metal ion concentration, and K_{SV}: Stern–Volmer quenching constant.

The plot indicates a complex quenching behavior. Initially, at concentrations up to 400 nM, a relatively linear relationship is observed (inset of Figure 3b), with a Stern–Volmer quenching constant estimated to be 0.0028 nM^{-1}. However, deviations from linearity become apparent at higher concentrations, suggesting a more complex quenching mechanism involving both static and dynamic quenching processes. To better represent this complexity, the data were fitted using a second-order polynomial equation:

$$\frac{F_0}{F} = K_D K_S [Q]^2 + [K_D + K_S]\,[Q] + 1 \tag{2}$$

where, F_0: initial fluorescence (no metal), F: fluorescence at a given metal concentration, $[Q]$: metal ion concentration, K_S: static quenching constant, and K_D: dynamic quenching constant.

This polynomial fit (Figure 3c) provides a more accurate representation of the observed quenching behavior.

$$y = 6.19 \times 10^{-6} x^2 + 1.43 \times 10^{-4} x + 1.215 \tag{3}$$

The linear term (1.43×10^{-4} nM) indicates that dynamic quenching dominates at lower metal concentrations. In contrast, the quadratic term (6.19×10^{-6}) suggests that static quenching or complex formation becomes more prominent at higher concentrations, possibly leading to a saturation effect [37, 38].

Furthermore, the sensitivity of the PQ probe toward Cu^{2+} detection was evaluated. The LOD was calculated using the values from the Stern–Volmer fit (Figure 3b), giving a value of 29 nM. This result confirms the high sensitivity of the PQ probe and its capability to detect Cu^{2+} at sub-micromolar levels. The results reveal a dual quenching behavior by the PQ sensor.

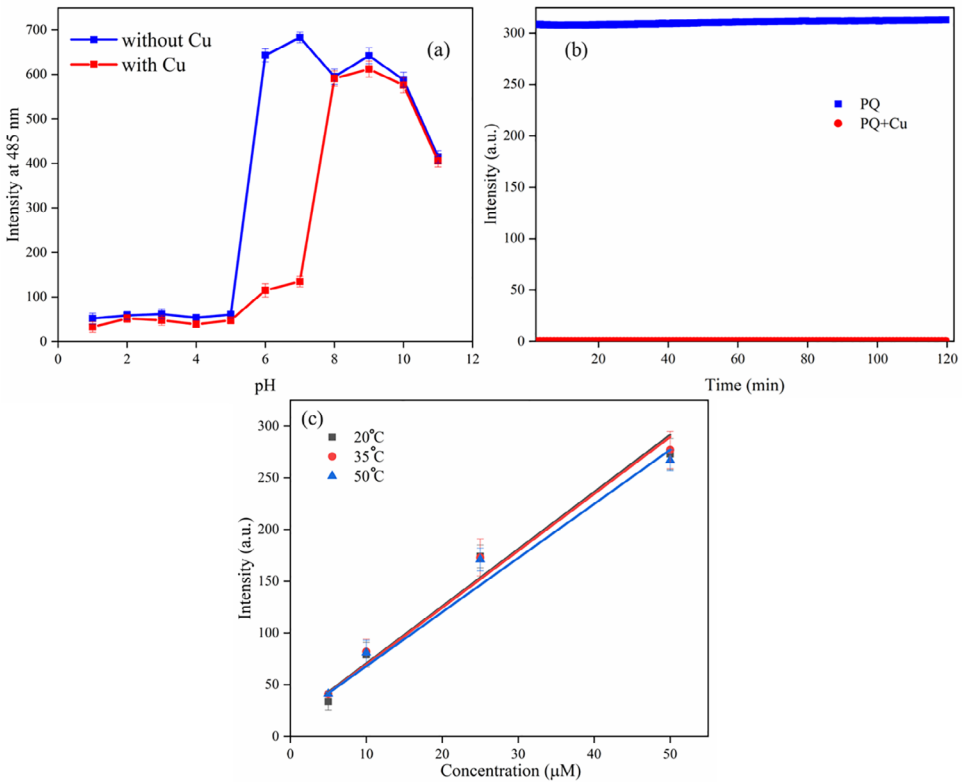

FIGURE 4 | (a) Effect of pH, (b) time-dependent fluorescence emission of PQ and PQ with the addition of 10 mM copper, and (c) temperature study of PQ at different concentrations at three different temperatures.

Dynamic quenching is prevalent at lower concentrations, while static quenching dominates as the metal concentration increases, likely due to complex formation or aggregation effects. This concentration-dependent shift in quenching mode, combined with PQ's nitrogen-rich binding sites and the influence of the ACN medium, supports a mechanism involving initial dynamic coordination followed by stable bidentate complex formation with Cu^{2+}.

3.4 | Influence on Sensor Dynamics: Effect of pH, Temperature, and Time

The effect of pH on the fluorescence behavior of PQ was investigated to identify optimal sensing conditions (Figure 4a). Under acidic conditions, PQ exhibited weak fluorescence even in the absence of Cu^{2+}, indicating protonation-induced quenching that limits effective sensing at low pH. As the pH increased to near-neutral conditions, the fluorescence intensity of PQ increased substantially; however, upon the addition of Cu^{2+}, a pronounced quenching response was observed. This behavior indicates effective coordination between PQ and Cu^{2+} under near-neutral conditions. At higher pH values, the fluorescence responses of PQ in the presence and absence of Cu^{2+} became nearly indistinguishable, suggesting that Cu^{2+} binding and the associated quenching process are suppressed under alkaline conditions. Based on these observations, pH 7 was selected as the optimal condition for Cu^{2+} sensing, as it provides a stable fluorescence baseline together with a clear and distinguishable response to Cu^{2+}. Similarly, the fluorescence intensity of both PQ and the PQ-copper solution remained unchanged over 120 min (Figure 4b). To assess the stability of the probe, varying concentrations of PQ were subjected to different temperatures, and the corresponding fluorescence intensities were measured (Figure 4c). The fluorescence intensity increased with higher PQ concentrations and remained stable across varying temperatures, indicating that the probe retains its performance even at elevated temperatures up to 50 °C.

3.5 | Influence on Sensor Dynamics: Effect of pH, Temperature, and Time

The binding interaction between ligand and the metal was studied using Job's plot, which displays a 1:1 stoichiometric ratio in between the metal and the PQ sensor (Figure 5a). This indicates that each PQ molecule coordinates with each Cu^{2+} to form PQ-Cu^{2+} complex. The mass spectrum of $[PQ+H]^+$ initially showed a signal peak at $m/z = 246$. After interaction with Cu^{2+}, a new signal peak for $[PQ + Cu^{2+} + NO_3^-]^+$ appeared at $m/z = 370$, demonstrating metal-ligand coordination (Figure S6). The interaction of the metal with the ligand was further studied using a series of fluorometric titrations (Figure 5b). The Benesi–Hildebrand (B–H) equation (Equation 4) was used to calculate the binding constant.

$$\frac{F_{max} - F_0}{F - F_0} = \frac{1}{K_b \times Conc.\,Cu^{2+}} + 1 \tag{4}$$

In this equation, F_0, F, and F_{max} represent the fluorescence emission intensities of PQ in the absence of Cu^{2+}, at an intermediate Cu^{2+} concentration, and at saturation concentration,

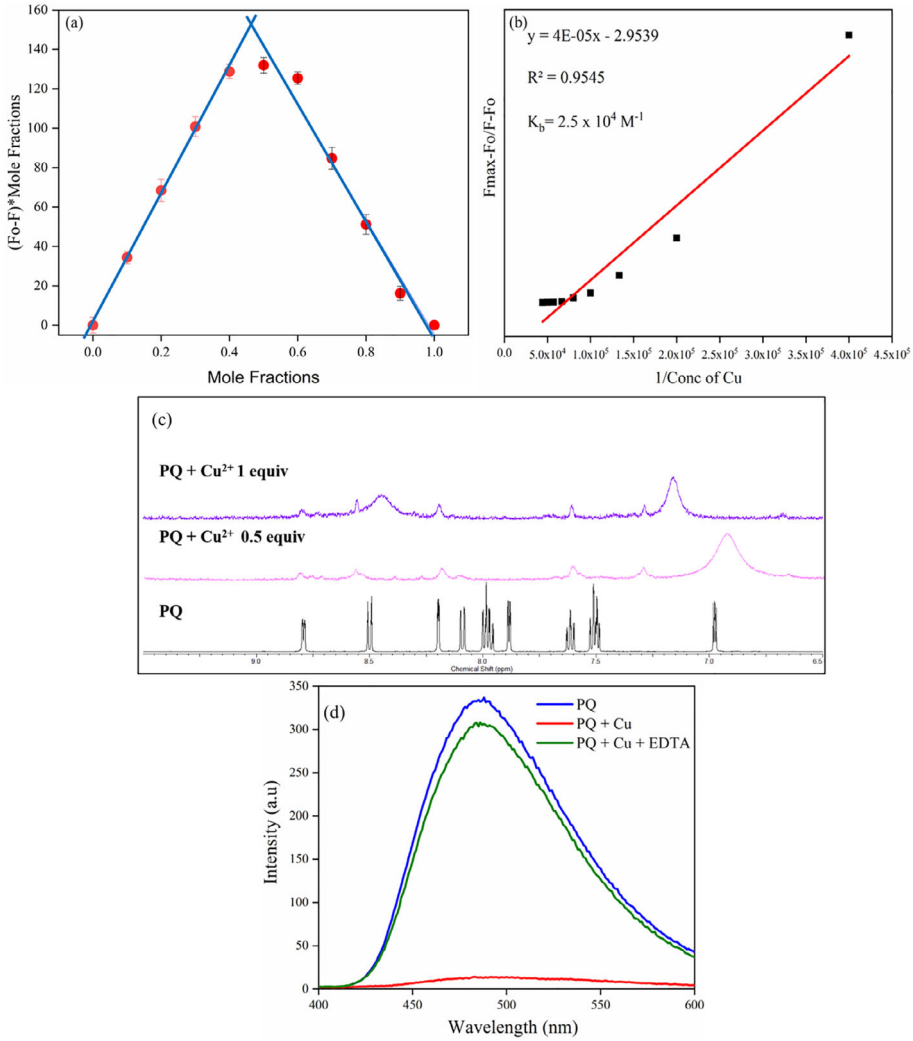

FIGURE 5 | (a) Job's plot, (b) Benesi–Hildebrand (B–H) plot, (c) ^{1}H NMR titration spectra (stacked) of PQ in the presence of Cu^{2+} at room temperature in CD_3CN, and (d) signal reversibility study with addition of EDTA in PQ-Cu solution.

respectively. K_b denotes the binding constant, and "$[Cu^{2+}]$" refers to the concentration of Cu^{2+} ions. The slope of the plot of $(F_{max}–F_0)/(F–F_0)$ versus Cu^{2+} concentration was used to determine the binding constant (K_b) which was estimated to be 2.5×10^4 M^{-1}, indicating a strong affinity between PQ and Cu^{2+}. This high K_b value suggests that the PQ sensor is highly sensitive to Cu^{2+} ions, making it ideal for detecting low concentrations. To further probe the interaction between PQ and Cu^{2+} ions, ^{1}H-NMR titration experiments were conducted (Figure 5c). Upon the addition of Cu^{2+} (0.5 and 1 equivalent) to the PQ solution, certain proton resonances exhibited slight downfield shifts. However, a well-resolved ^{1}H-NMR spectrum for the PQ-Cu^{2+} complex could not be obtained due to the paramagnetic nature of the Cu^{2+} (d^9) system, which also contributed to the reduced spectral resolution observed after Cu^{2+} addition [39, 40].

The reusability and stability of PQ are essential for confirming its effectiveness as a chemosensor. To evaluate this, EDTA was introduced into the PQ-Cu^{2+} complex, resulting in the restoration of fluorescence to its original intensity (Figure 5d). This occurs because EDTA chelates Cu^{2+}, releasing PQ and enabling recovery of its fluorescence properties, thereby demonstrating the sensor's reversible "on–off–on" behavior.

3.6 | Water Sample Analysis

Water samples collected from three distinct sources were analyzed for copper content using PQ as a fluorescent chemosensor, with the corresponding fluorescence emission spectra shown for each sample (Figure 6a). To validate the fluorescence-based quantification, copper concentrations were independently determined via AES, with the resulting calibration curve depicted in Figure 6b. Comparative analysis revealed a discrepancy of approximately 5% between the fluorescence-derived values and those obtained from AES, based on the calibration data and measured fluorescence intensities (Table S1).

3.7 | Cytotoxicity and Cell Imaging

The effect of the fluorescent sensor on Caco-2 cell viability was evaluated using the MTT assay following 48 h exposure to concentrations ranging from 5 to 50 μM (Figure 7a). Untreated controls and vehicle controls (1% ACN) showed comparable absorbance values (~1.00), confirming that the vehicle had no measurable impact on cell viability. Cells treated with 5 and 10 μM

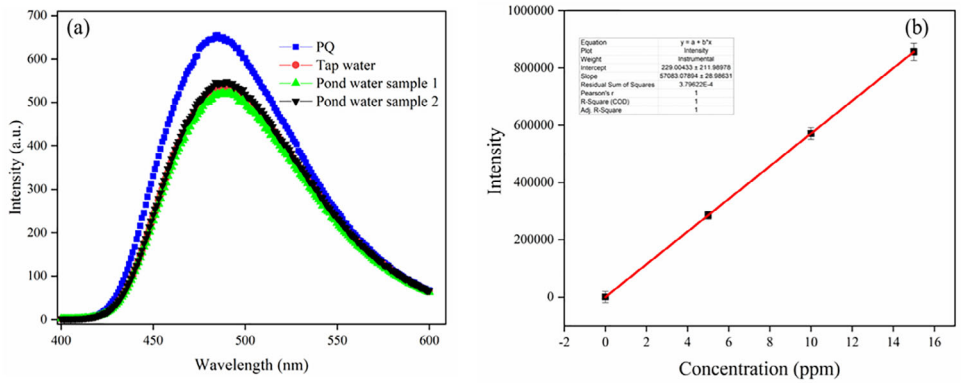

FIGURE 6 | (a) Fluorescence emission of water samples by addition of PQ and (b) calibration plot of copper standards obtained from AES.

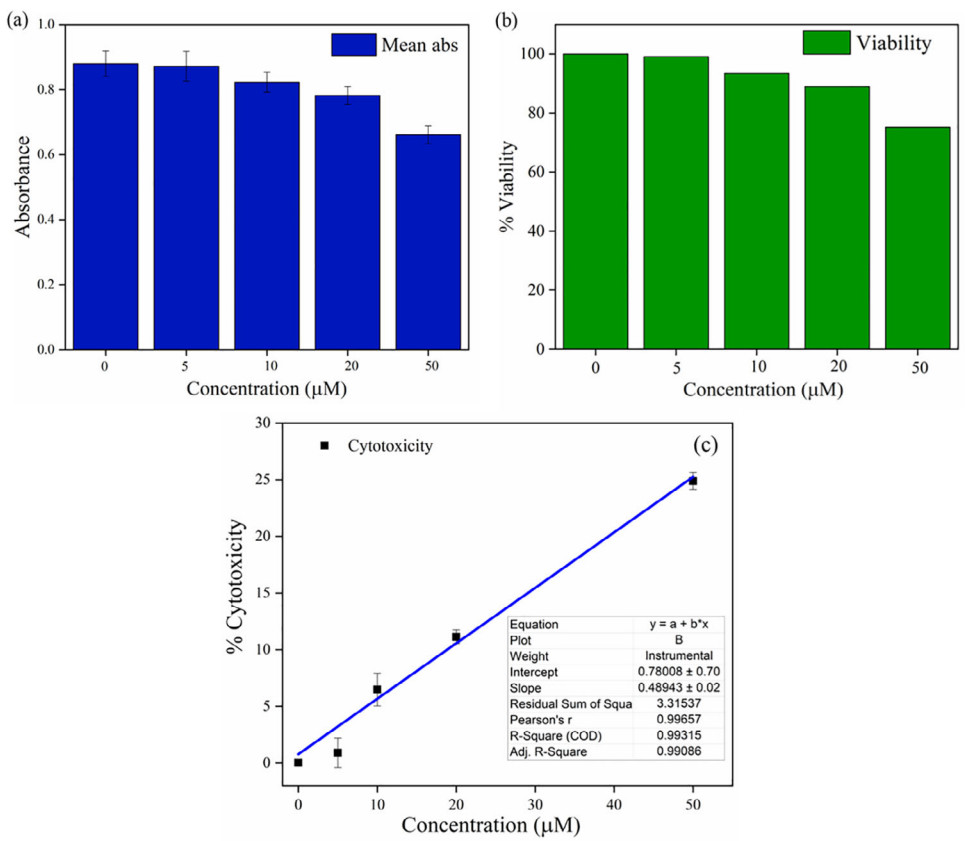

FIGURE 7 | Results of MTT assay following incubation of Caco-2 cells with PQ: (a) absorbance, (b) percent viability, and (c) linear regression analysis of cytotoxicity.

of the sensor maintained similar absorbance values to controls (0.99 ± 0.02 and 0.97 ± 0.03, respectively), indicating negligible cytotoxicity at these concentrations. At 20 μM, a modest reduction in absorbance was observed (0.91 ± 0.02), corresponding to approximately 89% viability relative to controls (Figure 7b). At the highest tested concentration of 50 μM, cell viability was markedly reduced (0.82 ± 0.03), representing approximately a 25% decrease compared to untreated cells.

Linear regression analysis of the concentration-response curve estimated an IC_{50} value of 98.77 μM, suggesting that the compound exhibits relatively low cytotoxicity in Caco-2 cells within the tested range (Figure 7c). The MTT assay results indicate that the fluorescent sensor is well tolerated at concentrations up to 10 μM, with minimal impact on cell viability after 48 h of treatment. However, higher concentrations (≥20 μM) induced a clear concentration-dependent reduction in viability, culminating in significantly decreased cell survival at 50 μM. These findings suggest that for biological imaging or sensor-based assays in Caco-2 cells, concentrations ≤10 μM are appropriate to minimize unwanted cytotoxic effects.

To investigate the interaction between copper ions (Cu^{2+}) and PQ, fluorescence microscopy was employed on Caco-2 cells treated

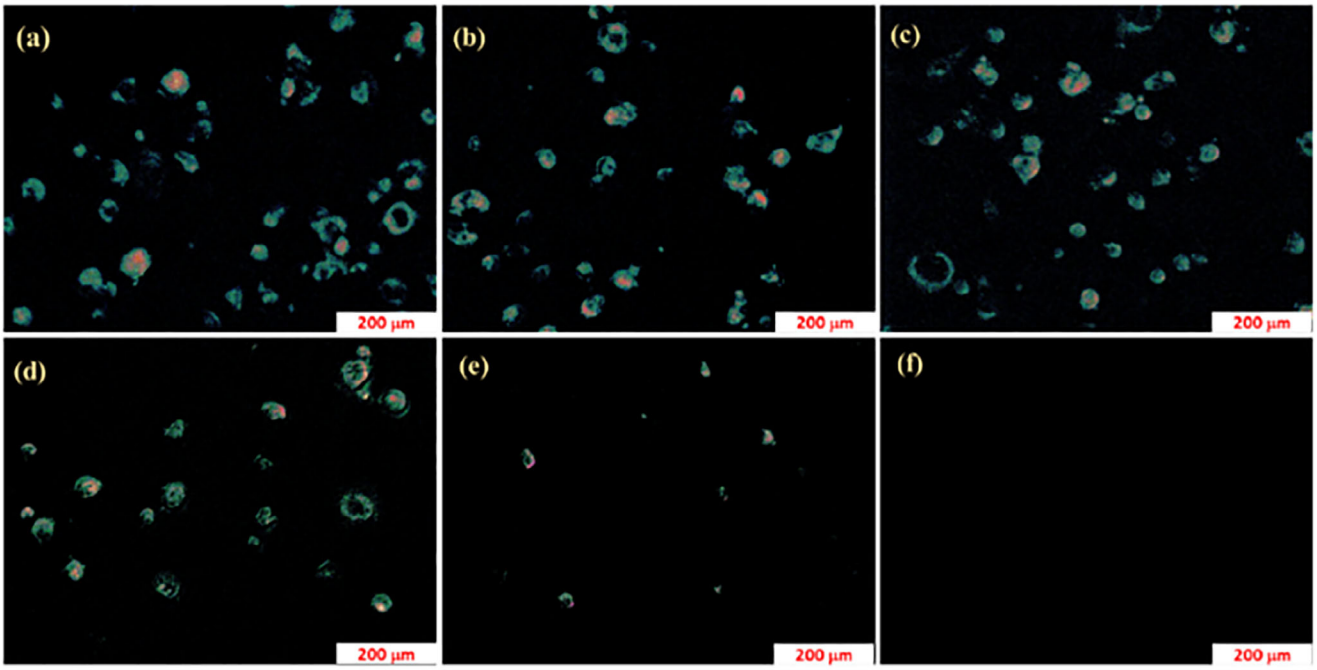

FIGURE 8 | Fluorescent images of PQ (5 mM) treated Caco-2 cells and incubated with Cu^{2+} of (a) 0, (b) 50, (c) 100, (d) 200, (e) 250, and (f) 300 nM, respectively.

with the probe in the presence of increasing concentrations of Cu^{2+} (0, 50, 100, 200, 250, and 300 nM). PQ exhibits fluorescence under standard conditions, but its emission intensity is known to be quenched upon coordination with copper. Fluorescence imaging was performed on PQ-labelled epithelial cells, and Figure 8 displays several regions corresponding to different copper concentrations. Visual inspection reveals a marked decrease in fluorescence intensity in regions exposed to higher concentrations of Cu^{2+}, confirming the concentration-dependent quenching behavior of PQ. At 50 nM Cu^{2+}, fluorescence intensity is still prominent, suggesting minimal binding and quenching. While at 100–250 nM Cu^{2+}, progressive quenching becomes evident, with reduced signal intensity across the cytoplasm. The unprocessed images of the cells can be seen in Figures S7 and S8. When the Cu^{2+} concentration reaches 300 nM, the fluorescence is significantly diminished, indicative of nearly complete quenching and efficient coordination of Cu^{2+} with PQ. This observed quenching trend is consistent with known photophysical interactions between metal ions and fluorophores, where metal coordination alters the electronic structure of the fluorophore, reducing its ability to fluoresce. The quenching behavior observed is likely attributable to static quenching, where a ground-state complex forms between PQ and Cu^{2+}. The efficiency of quenching, particularly at higher copper concentrations, suggests a strong binding interaction, supporting the hypothesis that PQ can act as a selective chemosensor for Cu^{2+} in biological systems. These results validate the functional utility of PQ as a fluorescence "turn-off" probe for copper ions in live-cell environments.

The fluorescence sensing behavior of PQ toward copper ions can be rationalized by considering its structural, electronic, and solvent-mediated interactions with Cu^{2+} in an ACN medium. PQ features nitrogen-donor atoms embedded in a rigid, planar quinoxaline framework, which inherently supports a bidentate coordination mode. Upon introduction of Cu^{2+}, a pronounced quenching of fluorescence is observed, attributed to the formation of a stable ground-state $[Cu(PQ)]^{2+}$ complex (Figure 9). Unlike the higher denticity coordination often observed for Cu^{2+}, the bidentate binding in this system is stabilized by the polar aprotic solvent ACN, which acts as a weak ligand. In solution, Cu^{2+} likely exists as a partially solvated species, $[Cu(ACN)_x(H_2O)_y]^{2+}$ ($x + y \approx 6$), where the ACN molecules occupy additional coordination sites [41, 42]. This solvation environment facilitates ligand exchange with PQ while sterically and kinetically restricting higher coordination numbers. At low Cu^{2+} concentrations (<400 nM), the Stern–Volmer plot exhibits a predominantly linear relationship, indicating dynamic quenching through collisional interactions between excited state PQ molecules and solvated Cu^{2+} ions. In this regime, no stable ground-state complex dominates, and fluorescence quenching arises from transient, non-radiative decay events. As the Cu^{2+} concentration increases beyond 400 nM, deviations from linearity emerge, signalling the increasing contribution of static quenching via stable PQ-Cu^{2+} complex formation. The [Ar] $3d^9$ configuration of Cu^{2+} predisposes the metal ion to Jahn–Teller distortion, producing either distorted square planar or elongated octahedral geometries. These geometries are compatible with PQ's donor atom positions, enhancing selective and strong binding. At elevated Cu^{2+} concentrations (>1000 nM), the fluorescence signal plateaus, suggesting complete complexation of PQ with Cu^{2+}, beyond which additional Cu^{2+} does not further quench the emission. The on–off–on reversibility of the system is confirmed by EDTA experiments, where EDTA effectively chelates Cu^{2+} from the PQ-Cu^{2+} complex, restoring the probe's fluorescence. This supports a nondestructive quenching mechanism dominated by coordination interactions rather than irreversible photophysical degradation.

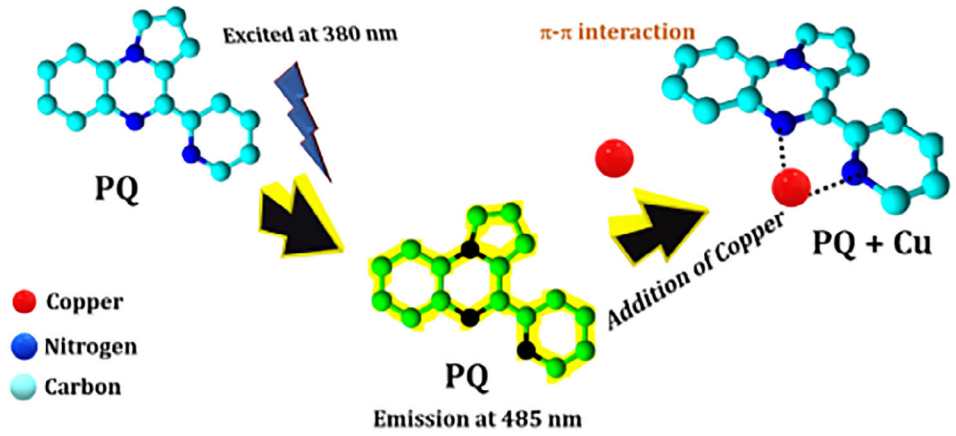

FIGURE 9 | Schematic illustration of copper sensing by PQ.

4 | Conclusion

These findings demonstrate that the PQ-based sensor operates through a robust and reversible metal-ligand interaction mechanism. Its selective response to Cu^{2+}, combined with strong binding affinity, fluorescence reversibility, and compatibility with aqueous and biological media, positions this PQ-based chemical sensor as a promising tool for environmental monitoring and analytical applications involving Cu^{2+} detection.

Acknowledgments

The authors thank London Metropolitan University for funding. The authors thank the EPSRC UK National Mass Spectrometry Facility at the Swansea University for high-resolution mass spectrometry analyses.

Conflicts of Interest

The authors declare no conflicts of interest.

Data Availability Statement

The data that support the findings of this study are available from the corresponding author upon reasonable request.

References

1. E. J. Ge, A. I. Bush, A. Casini, et al., "Connecting Copper and Cancer: From Transition Metal Signalling to Metalloplasia," *Nature Reviews Cancer* 22 (2022): 102–113, https://doi.org/10.1038/s41568-021-00417-2.

2. C. Zhong, J. Qiu, M. Liu, Y. Yuan, H. Zhu, and Y. Gao, "Rational Design and Bioimaging Application of Cholesterol Conjugated Fluorescence Probe for Cu^{2+} Detection," *Journal of Photochemistry and Photobiology A: Chemistry* 414 (2021): 113267, https://doi.org/10.1016/j.jphotochem.2021.113267.

3. R. Uauy, A. Maass, and M. Araya, "Estimating Risk From Copper Excess in Human Populations," *American Journal of Clinical Nutrition* 88 (2008): 867S–871S, https://doi.org/10.1093/ajcn/88.3.867S.

4. O. Bandmann, K. H. Weiss, and S. G. Kaler, "Wilson's Disease and Other Neurological Copper Disorders," *Lancet Neurology* 14 (2015): 103–113, https://doi.org/10.1016/S1474-4422(14)70190-5.

5. R. Kriss and M. A. Edwards, "Guidance for Residents Addressing Copper Problems in Drinking Water: Opportunities and Challenges," *ACS ES&T Water* 4 (2024): 4175–4183, https://doi.org/10.1021/acsestwater.4c00447.

6. Y. Wang, Q. Yan, Y. Shi, and M. Long, "Copper Toxicity in Animals: A Review," *Biological Trace Element Research* 203 (2025): 2675–2686, https://doi.org/10.1007/s12011-024-04345-8.

7. J. T. Trevors and C. M. Cotter, "Copper Toxicity and Uptake in Microorganisms," *Journal of Industrial Microbiology & Biotechnology* 6 (1990): 77.

8. A. Takami and K. Uchino, "Discovering the Hidden Link: Hematological Disorders Caused by Copper Deficiency," *International Journal of Hematology* 122 (2025): 358–367, https://doi.org/10.1007/s12185-025-04036-7.

9. G. Singh and S. Sharma, "Heavy Metal Contamination in Fish: Sources, Mechanisms and Consequences," *Aquatic Sciences* 86 (2024): 107, https://doi.org/10.1007/s00027-024-01121-7.

10. J. Alagan, R. Sarika, and A. Sumithra Devi, "A Fluorescent Probe Derived From L-Tryptophan for Copper (II) Ion Detection in Aqueous Media," *ChemistrySelect* 9 (2024): e202401026.

11. P. Purkayastha, "Cu^{2+} Induced Charge Transfer Switch by Choosing the Right Cyclodextrin Environment," *Journal of Photochemistry and Photobiology A: Chemistry* 212 (2010): 43–48, https://doi.org/10.1016/j.jphotochem.2010.03.013.

12. H. Zhu, M. Liu, C. Liu, et al., "Portable Ratiometric Fluorescence Analytical Device for Copper Ions Based on Smartphone in Environment and Living Organisms," *Science of the Total Environment* 857 (2023): 159488, https://doi.org/10.1016/j.scitotenv.2022.159488.

13. S. Mandal, S. Pu, L. He, H. Ma, and D. Hou, "Biochar Induced Modification of Graphene Oxide & nZVI and Its Impact on Immobilization of Toxic Copper in Soil," *Environmental Pollution* 259 (2020): 113851, https://doi.org/10.1016/j.envpol.2019.113851.

14. G. Doner and A. Ege, "Determination of Copper, Cadmium and Lead in Seawater and Mineral Water by Flame Atomic Absorption Spectrometry After Coprecipitation With Aluminum Hydroxide," *Analytica Chimica Acta* 547 (2005): 14–17, https://doi.org/10.1016/j.aca.2005.02.073.

15. J. S. Becker, A. Matusch, C. Depboylu, J. Dobrowolska, and M. V. Zoriy, "Quantitative Imaging of Selenium, Copper, and Zinc in Thin Sections of Biological Tissues (Slugs—Genus Arion) Measured by Laser Ablation Inductively Coupled Plasma Mass Spectrometry," *Analytical Chemistry* 79 (2007): 6074–6080, https://doi.org/10.1021/ac0700528.

16. A. M. Hernández-Martínez, C. Padrón-Sanz, M. E. Torres-Padrón, Z. Sosa-Ferrera, and J. J. Santana-Rodríguez, "Analysis of Ni, Cr, Cu, Pb and Cd in Marine Bioindicators Using Mixed-Micelles With Microwave Assisted Micellar Extraction and GF-AAS," *Analytical Methods* 8 (2016): 7141–7149, https://doi.org/10.1039/C6AY01913G.

17. W. Zhang, M. Li, X. Wang, et al., "Precision Navigation of Venous Thrombosis Guided by Viscosity-Activatable Near-Infrared

Fluorescence," *Analytical Chemistry* 95 (2023): 2382–2389, https://doi.org/10.1021/acs.analchem.2c04395.

18. J.-T. Chen, S.-S. Chen, Z.-Q. Wang, et al., "Near-Infrared Fluorescent Nanoprobes for Adenosine Triphosphate-Guided Imaging in Cancer and Fatty Liver Mice," *Analytical Chemistry* 95 (2023): 2119–2127, https://doi.org/10.1021/acs.analchem.2c05235.

19. K. Wang, Y. Liu, C. Liu, et al., "A New-Type HOCl-Activatable Fluorescent Probe and Its Applications in Water Environment and Biosystems," *Science of the Total Environment* 839 (2022): 156164, https://doi.org/10.1016/j.scitotenv.2022.156164.

20. H. Kang, W. Shu, J. Yu, et al., "Endoplasmic Reticulum-Targeted Two-Photon Fluorescent Probe for the Detection of Nitroxyl in a Parkinson's Disease Model," *Analytical Chemistry* 95 (2023): 6295–6302, https://doi.org/10.1021/acs.analchem.2c05127.

21. H. Zhu, P. Jia, X. Wang, et al., "In Situ Observation of Lysosomal Hypobromous Acid Fluctuations in the Brain of Mice With Depression Phenotypes by Two-Photon Fluorescence Imaging," *Analytical Chemistry* 94 (2022): 11783–11790, https://doi.org/10.1021/acs.analchem.2c01884.

22. J. Liu, M. Zhao, F. Zhao, X. Song, and Y. Ye, "ONOO–Triggered Fluorescence H_2S Donor for Mitigating Drug-Induced Liver Injury," *Sensors and Actuators B: Chemical* 378 (2023): 133131, https://doi.org/10.1016/j.snb.2022.133131.

23. Y. Zheng, Z. Ye, X. Zhang, and Y. Xiao, "Recruiting Rate Determines the Blinking Propensity of Rhodamine Fluorophores for Super-Resolution Imaging," *Journal of the American Chemical Society* 145 (2023): 5125–5133, https://doi.org/10.1021/jacs.2c11395.

24. M. Liu, H. Zhu, K. Wang, et al., "A Novel Fluorescent Chemodosimeter for Discriminative Detection of Cu^{2+} in Environmental, Food, and Biological Samples," *ACS Food Science & Technology* 3 (2023): 134–140, https://doi.org/10.1021/acsfoodscitech.2c00329.

25. A. Aziz, M. Asif, G. Ashraf, et al., "Boosting Electrocatalytic Activity of Carbon fiber@ Fusiform-Like Copper-Nickel LDHs: Sensing of Nitrate as Biomarker for NOB Detection," *Journal of Hazardous Materials* 422 (2022): 126907, https://doi.org/10.1016/j.jhazmat.2021.126907.

26. M. Asif, G. Ashraf, A. Aziz, et al., "Tuning the Redox Chemistry of Copper Oxide Nanoarchitectures Integrated With rGOP via Facet Engineering: Sensing H_2S Toward SRB Detection," *ACS Applied Materials & Interfaces* 14 (2022): 19480–19490, https://doi.org/10.1021/acsami.2c02119.

27. M. Asif, Z. Wang, A. Aziz, et al., "Hybridizing $Ti_3C_2T_x$ Layers With Layered Double Hydroxide Nanosheets at the Molecular Level: A Smart Electrode Material for H_2 O_2 Monitoring in Cancer Cells," *ACS Applied Materials & Interfaces* 15 (2023): 32075–32086, https://doi.org/10.1021/acsami.3c02004.

28. A. Karpe, A. Parab, G. Ganesan, P. Walke, and A. Chaskar, "Highly Conjugated Carbazole and Pyrrolo [1, 2-a] Quinoxaline Based Small Molecules for Fluorescent Detection of Nitroexplosives," *Journal of Photochemistry and Photobiology A: Chemistry* 431 (2022): 114004, https://doi.org/10.1016/j.jphotochem.2022.114004.

29. A. Karpe, A. Parab, G. Ganesan, J. Lade, P. Walke, and A. Chaskar, "Highly Emissive Pyrrolo [1, 2-a] Quinoxaline Based Narrow Band Fluorescent Sensors for Detection of Nitroaromatics and Their Application in Spot Paper Test," *Chemical Physics Impact* 8 (2024): 100568, https://doi.org/10.1016/j.chphi.2024.100568.

30. S. Gemma, L. Colombo, G. Forloni, et al., "Pyrroloquinoxaline Hydrazones as Fluorescent Probes for Amyloid Fibrils," *Organic & Biomolecular Chemistry* 9 (2011): 5137, https://doi.org/10.1039/c1ob05288h.

31. L. Zaccagnini, S. Brogi, M. Brindisi, et al., "Identification of Novel Fluorescent Probes Preventing PrPSc Replication in Prion Diseases," *European Journal of Medicinal Chemistry* 127 (2017): 859–873, https://doi.org/10.1016/j.ejmech.2016.10.064.

32. K. M. Divya, D. P. Savitha, G. Anjali Krishna, T. M. Dhanya, and P. V. Mohanan, "A Thiophene Based Pyrrolo [1, 2-a] Quinoxaline Fluorescent Probe as a "Turn-off" Sensor for the Selective Nanomolar Detection of Sodium Ion," *Journal of Photochemistry and Photobiology A: Chemistry* 431 (2022): 114046, https://doi.org/10.1016/j.jphotochem.2022.114046.

33. M. Damai, N. Guzzardi, V. Lewis, Z. X. Rao, D. Sykes, and B. Patel, "Crafting Mono-and Novel Bis-methylated Pyrroloquinoxaline Derivatives From a Shared Precursor and Its Application in the Total Synthesis of Marinoquinoline A," *RSC Advances* 13 (2023): 29561–29567, https://doi.org/10.1039/D3RA05952A.

34. X. Xu, C. Wang, O. Bäcke, et al., "Pyrrolo [3, 4-g] Quinoxaline-6, 8-dione-Based Conjugated Copolymers for Bulk Heterojunction Solar Cells With High Photovoltages," *Polymer Chemistry* 6 (2015): 4624–4633, https://doi.org/10.1039/C5PY00394F.

35. D. Reinen In, *Vibronic Processes in Inorganic Chemistry*, ed. C. D. Flint, (Springer, 1989), 267–282, https://doi.org/10.1007/978-94-009-1029-4.

36. K. Mack, A. Wünsche von Leupoldt, C. Förster, et al., "Effect of Chelate Ring Expansion on Jahn-Teller Distortion and Jahn-Teller Dynamics in Copper (II) Complexes," *Inorganic Chemistry* 51 (2012): 7851–7858, https://doi.org/10.1021/ic300929g.

37. A. S. Tanwar, R. Parui, R. Garai, M. A. Chanu, and P. K. Iyer, "Dual "Static and Dynamic" Fluorescence Quenching Mechanisms Based Detection of TNT via a Cationic Conjugated Polymer," *ACS Measurement Science Au* 2 (2022): 23–30, https://doi.org/10.1021/acsmeasuresciau.1c00023.

38. D. Genovese, M. Cingolani, E. Rampazzo, L. Prodi, and N. Zaccheroni, "Static Quenching Upon Adduct Formation: A Treatment Without Shortcuts and Approximations," *Chemical Society Reviews* 50 (2021): 8414–8427, https://doi.org/10.1039/D1CS00422K.

39. H. Karabıyık, Ö. Erdem, M. Aygün, and M. A. Chanu, "Ligand-to-Metal Charge Transfer Resulting in Metalloaromaticity of [R, R-Cyclohexyl-1, 2-bis (2-Oxidonaphthylideneiminato-N, N', O, O')] Cu (II): A Scrutinized Structural Investigation," *Journal of Inorganic and Organometallic Polymers* 20 (2010): 142.

40. P. Mukherjee, M. G. B. Drew, A. Figuerola, and A. Ghosh, "Incorporation of a Sodium Ion Guest in the Host of Copper (II)-Schiff-Base Complexes: Structural Characterization and Magnetic Study," *Polyhedron* 27 (2008): 3343–3350, https://doi.org/10.1016/j.poly.2008.07.025.

41. P. D'Angelo and V. Migliorati, "Solvation Structure of Zn^{2+} and Cu^{2+} Ions in Acetonitrile: A Combined EXAFS and XANES Study," *Journal of Physical Chemistry B* 119 (2015): 4061.

42. Z. Wu, Y. Li, A. Amardeep, et al., "Unveiling the Mysteries: Acetonitrile's Dance With Weakly-Solvating Electrolytes in Shaping Gas Evolution and Electrochemical Performance of Zinc-Ion Batteries," *Angewandte Chemie International Edition* 63 (2024): e202402206, https://doi.org/10.1002/anie.202402206.

Supporting Information

Additional supporting information can be found online in the Supporting Information section.

The authors have cited additional references within the Supporting Information [30, 31].

Supporting File 1: slct73902-sup-0001-SuppMat.docx